



Electric-field-induced multiferroic topological solitons

Arthur Chaudron, Zixin Li, Aurore Finco, Pavel Marton, Pauline Dufour,
Amr Abdelsamie, Johanna Fischer, Sophie Collin, Brahim Dkhil, Jirka
Hlinka, et al.

► To cite this version:

Arthur Chaudron, Zixin Li, Aurore Finco, Pavel Marton, Pauline Dufour, et al.. Electric-field-induced multiferroic topological solitons. *Nature Materials*, In press, 10.1038/s41563-024-01890-4 . hal-04604964

HAL Id: hal-04604964

<https://hal.science/hal-04604964>

Submitted on 7 Jun 2024

HAL is a multi-disciplinary open access archive for the deposit and dissemination of scientific research documents, whether they are published or not. The documents may come from teaching and research institutions in France or abroad, or from public or private research centers.

L'archive ouverte pluridisciplinaire **HAL**, est destinée au dépôt et à la diffusion de documents scientifiques de niveau recherche, publiés ou non, émanant des établissements d'enseignement et de recherche français ou étrangers, des laboratoires publics ou privés.

Electric-field induced multiferroic topological solitons

Arthur Chaudron¹, Zixin Li², Aurore Finco³, Pavel Marton^{4,5}, Pauline Dufour¹, Amr Abdelsamie^{1,3}, Johanna Fischer¹, Sophie Collin¹, Brahim Dkhil⁶, Jirka Hlinka⁴, Vincent Jacques³, Jean-Yves Chauleau², Michel Viret², Karim Bouzehouane¹, Stéphane Fusil^{1,7*}, Vincent Garcia^{1*}

¹Laboratoire Albert Fert, CNRS, Thales, Université Paris-Saclay, 91767 Palaiseau, France

²SPEC, CEA, CNRS, Université Paris-Saclay, 91191 Gif-sur-Yvette, France

³Laboratoire Charles Coulomb, Université de Montpellier and CNRS, 34095 Montpellier, France

⁴Institute of Physics, Academy of Sciences of the Czech Republic, Na Slovance 2, 18221 Praha 8, Czech Republic

⁵Institute of Mechatronics and Computer Engineering, Technical University of Liberec, Studentská 2, 461 17 Liberec, Czech Republic

⁶Université Paris-Saclay, CentraleSupélec, CNRS, Laboratoire SPMS, 91190, Gif-sur-Yvette, France

⁷Université d'Evry, Université Paris-Saclay, 91000 Evry, France

*email: stephane.fusil@cnrs-thales.fr, vincent.garcia@cnrs-thales.fr

Topologically-protected spin whirls in ferromagnets are foreseen as the carthorse of solitonic information technologies. Nevertheless, the future of skyrmionics may rely on antiferromagnets due to their immunity to dipolar fields, straight motion along the driving force, and ultrafast dynamics. While complex topological objects were recently discovered in intrinsic antiferromagnets, mastering their nucleation, stabilization, and manipulation with energy-efficient means remains an outstanding challenge. Designing topological polar states in magnetoelectric antiferromagnetic multiferroics would allow one to electrically write, detect and erase topological antiferromagnetic entities. Here we stabilize ferroelectric center states using a radial electric field in multiferroic BiFeO₃ thin films. We show that such polar textures contain flux closures of antiferromagnetic spin cycloids, with distinct antiferromagnetic entities at their cores depending on the electric-field polarity. By tuning the epitaxial strain, quadrants of canted antiferromagnetic domains can also be electrically designed. These results open the path to reconfigurable topological states in multiferroic antiferromagnets.

Topological polar objects are now emerging¹ with experimental demonstrations of polar vortices, skyrmions and center states in ferroelectric-based superlattices^{2,3}, thin films^{4,5} and nanostructures⁶⁻⁸. These entities can be scaled down to nanometer sizes, controlled with energy-efficient electric fields, and detected via non-destructive resistive readout, making them interesting for information technologies and in particular memory applications. Among them, topological center-type domains in ferroelectric thin films are currently garnering attention for their stability, switchability and electrical conduction properties^{9,7,6,10,8,11}. Topological defects here refer to local singularity regions in an ordered medium wherein the

order parameter ceases to vary continuously¹². Both center-convergent (head-to-head) or center-divergent (tail-to-tail) polar states are characterized by a finite winding number of +1 in a two-dimensional projection^{6,12}, which might provide some topological protection. However, the lack of a full rotation of polarization in the third dimension prevents the topological charge to be ± 1 , as is the case for skyrmions in the homotopy group $\pi_2(S^2)$. Such center convergent or divergent polar textures have been reported in spatially confined nanoscale structures such as as-grown pillars in the bottom-up approach^{7,10}, or in etched islands in the top-down approach⁸ in BiFeO₃ thin films. They were also shown to display different electrical states, with resistances contrasting by several orders of magnitude^{7,8,11}, paving the way for ferroelectric topological resistive memories. However, the behavior of their coupled antiferromagnetic order remains an uncharted territory.

Controlling spin textures in antiferromagnetic materials is intrinsically challenging due to their insensitivity to magnetic fields. This has been reported to be feasible, taking advantage of the magnetoelectric coupling¹³, in the room-temperature multiferroic BiFeO₃, harboring ferroelectricity and a G-type antiferromagnetic order superimposed with a spin cycloid^{14,15}. A comprehensive description of the BiFeO₃ magnetic ordering can be found in the review by Burns et al.¹⁶ and references therein. Indeed, ferroelectric textures in BiFeO₃ thin films have been shown to imprint their antiferromagnetic order^{13,17,18}. Depending on epitaxial strain, electric fields were shown to either provide a deterministic control of the spin cycloid propagation¹³ or to change the antiferromagnetic order from canted collinear G-type textures to spin cycloids¹⁷.

Here we report on the coupled polar and antiferromagnetic topological nanoscale textures induced by electric-field pulses in submicron devices based on BiFeO₃ thin films under various epitaxial strains. When subjected to compressive epitaxial strain, we show how ferroelectric

center domains yield flux closures of antiferromagnetic spin cycloids, while magnetic simulations give credence to the occurrence of antiferromagnetic singularities at their very center. When subjected to tensile epitaxial strain, we show how those same ferroelectric center domains lead to four-quadrant homogeneous canted antiferromagnetic spin textures. In both cases, we observe a “one-to-one” imprint of the ferroelectric domains into the antiferromagnetic ones, albeit multiple antiferromagnetic states are in principle energetically degenerate for a single ferroelectric domain. This “simple” magnetoelectric coupling holds promise for devices based on topology in multiferroic BiFeO₃, allowing deterministic electrical switching of antiferromagnetic ordering.

As previously reported¹¹, applying radial electric fields between a patterned top electrode and a conductive tip (Fig. 1b) has proven to be an effective and reproducible method to induce ferroelectric center states in (001)-oriented BiFeO₃ thin films. Four-quadrants center-convergent (Fig. 1a) and center-divergent (Fig. 1c) polar textures can be written by electric pulses of opposite signs.

Conversely to bulk, where cycloids can propagate along three energetically-equivalent crystallographic directions coupled to the ferroelectric polarization¹⁹, this degeneracy is lifted by epitaxial strain in such thin films and the cycloid propagating purely in the film plane is selected¹³. Such a behavior implies that any rotation of the ferroelectric polarization imprints an equivalent rotation of the cycloid propagation direction, while preserving the clockwise (Fig. 1d), or counter-clockwise (Fig. 1g) rotation of the antiferromagnetic spins alongside it, if a single magnetic polarity is considered²⁰. Indeed, a convenient way to describe the spin cycloid in BiFeO₃ is to refer to its magnetic polarity²⁰: this quadratic order parameter is defined as $\lambda = k \times S_i \times S_j$, where S_i and S_j are spins on adjacent i and j sites along the cycloidal propagation direction k . This magnetic polarity unambiguously determines the sense of

rotation or handedness of the spin cycloid. It couples to the polarization P through an energy term proportional to $\lambda \cdot P$ in the Landau expansion. Incidentally, a single magnetic polarity (antiparallel to the polarization vector) has been detected within a defined polar domain experimentally, in both single crystals²¹ and thin films^{20,22}. Hence, we will in the following consider the magnetic polarity vector to be antiparallel to the polarization within each ferroelectric variant. Thus, all symmetries pertaining to ferroelectric textures should hold for their antiferromagnetic counterparts, and it becomes possible to rely on the magnetoelectric coupling to induce antiferromagnetic topological states anchored on ferroelectric center domains.

Considering these polar topological textures and the magnetoelectric coupling, we ran atomistic simulations of the spin textures for the upwards center-convergent and downwards center-divergent ferroelectric states. In both cases, in addition to the pristine cycloidal rotation of the spins within single domains, another full in-plane rotation is induced at the core of the four-quadrant states, corresponding to the antiferromagnetic equivalents of hedgehog vortices (Fig. 1f) and antivortices (Fig. 1e)²³. These unique spin textures are confined at the junction of several unidirectional k -vectors, which are an essential prerequisite to the emergence of antiferromagnetic skyrmion-like features that have not been reported yet. Controlling these antiferromagnetic singularities with an electric-field is a paramount asset of BiFeO₃.

Results

Polar mapping and writing

Since the ferroelectric textures are defined as fields of 3D vectors, the need arises to display the dataset in the simplest way to showcase the nature of the electrically-poled polar landscape. In this mindset, Fig. 2 provides insights on the process used to extract a polar map from PFM phase and amplitude measurements. Similar processing and visualization of PFM data has already been used in the literature^{6,8,24} and coined as “vector PFM”.

In this typical example, a ferroelectric center convergent domain state was stabilized in a 800-nm-wide BiFeO₃ device confined by a Pt circular electrode (Fig. 2a), when the AFM tip was placed at the center of the device to apply a radial electric field. The vertical piezoresponse force microscopy (VPFM) indicates a uniform signal, corresponding to a polarization pointing upwards (Fig. 2b). The lateral piezoresponse force microscopy (LPFM) responses show a splitting of the bare BiFeO₃ disk into two halves when the cantilever is aligned vertically (Fig. 2c), as well as when the cantilever is aligned horizontally (Fig. 2d). The LPFM signals collected at different angles allow the reconstruction of the vector polarization map from the local direction and magnitude of the LPFM responses triggered by electrical excitation in this peculiar design lacking any bottom electrode (a few volts AC bias is applied between the surrounding electrode and the grounded tip to trigger the piezoresponse, see Fig. 1b).

The underlying ferroelectric polar texture is approximated by projecting the 3D piezoresponse vectors to the closest crystallographic axes allowed for the dipole moment. The resulting ferroelectric domain mappings are illustrated by the overlaid color scales (Fig. 2e-f). Some examples of full lateral piezoresponse characterizations, obtained before applying the azimuthal angle projection, are provided in Supplementary Fig. 1. Taking advantage of this systematic data processing, all further atomistic magnetic simulations will be based on such

polar vector maps, deduced from actual experimentally-designed and measured ferroelectric textures.

Flux-closure antiferromagnetic spin cycloids

When subjected to -0.35% compressive strain, i.e. thanks to epitaxial growth on DyScO₃ substrates, BiFeO₃ has been shown to retain its bulk-like antiferromagnetic spin cycloid^{13,17,18}.

In the pristine state, all thin films studied here exhibit a stripy ferroelectric texture consisting of two alternating polarization variants (Fig. 3a) separated by 71° domain walls, and corresponding to the two favored ferroelastic variants. This anisotropy stems from the monoclinic distortion transferred from the (110) scandate substrate to BiFeO₃ (Ref. 25). Each domain is harboring a single cycloid propagating in the film plane and in a direction k_1 (green double arrows in Fig. 3d), and giving rise to the zig-zag magnetic pattern (Fig. 3g), as previously reported^{13,17,18}. The aforementioned magnetic polarity λ is defined within each ferroelectric domain as a green arrow antiparallel to the polarization (Fig. 3d). The two other, non-pre-existing and least stable, ferroelastic variants that are created in center states (Fig. 3b-c) are prone to relax to some extent. However, the four quadrant textures' cores, which contain the topological information, were found to be stable for months. Fig. 3b is a typical example of a divergent center state that underwent minor relaxation, restricted to the edges of the device. The two switchable states are expected to yield opposite rotations of the spin cycloid in all quadrants (Fig. 3e-f), as a single magnetic polarity has been demonstrated for a given polarization²⁰⁻²². This induces two distinct senses of rotation and for the antiferromagnetic spin cycloids around the texture centers.

The corresponding magnetic stray field maps, as deduced from scanning nitrogen-vacancy (NV) magnetometry (Methods, Supplementary Fig. 2), are displayed in Fig. 3h-i and nicely corroborate the overall expected antiferromagnetic patterns by displaying four cycloidal directions, rotated one from the other by 90° at each domain wall. These results are highlighting the sharp correlation between ferroelectric and antiferromagnetic domains, whose respective walls overlap perfectly within the resolution limits of these near-field experiments.

Supplementary Fig. 3 presents similar magnetometry measurements performed on center-divergent ferroelectric states that were induced on identical disk patterns through the same writing process, attesting for such textures' reproducibility and stability. Although the stitching of antiferromagnetic spin cycloids at domain walls appears to vary from one device to another, the propagation direction of those cycloids in each quadrant is fully deterministic and was found to remain stable, at least for weeks.

Moreover, Fig. 3j-k show simulated results for the antiferromagnetic spin textures coupled to the actual center polar states. As previously mentioned, the underlying ferroelectric states were initialized based on the experimental polar domain maps provided by PFM measurements (as in Fig. 2). Scanning NV magnetometry images are reproduced quite reliably, at least regarding their overall topology, since the stitching at domain walls was found to depend on the initial antiferromagnetic state used in the simulations. The insets provide a zoom-in on individual spins around the cores of the two center polar states and give credence to the local stabilization of two distinct antiferromagnetic singularities, although their existence cannot be corroborated experimentally due to a lack of resolution.

Pseudo-collinear G-type antiferromagnetic quadrants

When subjected to +0.50% tensile strain, i.e. thanks to epitaxial growth on SmScO_3 substrates, BiFeO_3 has been shown to destabilize its bulk-like spin cycloid, yielding a pseudo-collinear G-type antiferromagnetic ordering^{17,26,27}. In BiFeO_3 , the investigation on the local coupling between ferroelectric polarization and pseudo-collinear G-type antiferromagnetic domains has been very shallow, with no clear experimental report to the best of our knowledge. It was still reported that the antiferromagnetic vector L_i in such domains could only lie along three energetically-equivalent crystallographic directions coupled to the ferroelectric polarization²⁸. Those three directions happen to be the same as the aforementioned bulk-like spin cycloid propagation directions that belong to the pseudo-cubic (111) plane perpendicular to the polarization (Supplementary Fig. 4a)²⁸. In turn, when the cycloid is destroyed, the second Dzyaloshinskii-Moriya interaction, related to the oxygen octahedra tilts along the polarization direction²⁹, gives rise to a net canted magnetization $\pm M_i$ along the direction perpendicular to both the antiferromagnetic Néel vector L_i and the ferroelectric polarization P (Supplementary Fig. 4b-c)^{26,28}. Taking its sign into account, this weak moment can then lie along six possible orientations within a given ferroelectric domain.

The pristine polar landscape of the films grown on SmScO_3 is similar to the previously described compressive strain case (Fig. 4a). Fig. 4d shows how the pseudo-collinear G-type antiferromagnetic domains overlap their ferroelectric counterparts in as-grown BiFeO_3 under tensile strain. It seems that the net magnetization stays uniform within each ferroelectric monodomain, and exhibits two distinct alternating configurations coupled to the ferroelectric stripes. Micromagnetic simulations were run considering a uniform net magnetization pointing in any of the 6 permitted crystallographic directions within each experimentally-measured ferroelectric domain (Supplementary Note 1). This allows us to compute the

magnetic stray field landscape radiated at the NV center height for all possible canted moment configurations, and to identify the ones experimentally observed. The results are depicted in the schematics of Fig. 4g, indicating that both ferroelectric variants contain the same magnetic variant M_3 (more information in Supplementary Fig. 5). However, this local one-to-one correspondence behavior does not always yield at larger scale, where patches of different alternating configurations may be observed (Supplementary Fig. 6). Comparing these large-scale NV images with simulations (Supplementary Fig. 7), we identify up to two magnetic variants M_3 and M_2 being harbored in each ferroelectric domain.

Nonetheless, the local “one-to-one” magnetoelectric coupling was found to be retained through electrical writing of center domains, as exhibited by Fig. 4e-f, where scanning NV magnetometry images show either the highest field or highest field gradient at the approximate location of the ferroelectric domain walls (more information in Supplementary Fig. 8 and Supplementary Fig. 9). Both center-convergent (Fig. 4b) and center-divergent (Fig. 4c) polar textures thus imprinted a single antiferromagnetic domain over each of their quadrants. In order to identify the actual canted moment configurations, magnetic-field simulations were again performed from all 6^4 configurations a priori permitted by the center domains. Out of all those simulated configurations, a single one qualitatively matched scanning NV magnetometry measurements for the downwards center-divergent ferroelectric texture, and is illustrated in Fig. 4h. Supplementary Fig. 8 presents the comparison of the measured and simulated magnetic field along the three cartesian axes for this specific net magnetization configuration.

This matching process was found to be more cumbersome for the downwards center-convergent ferroelectric texture. Supplementary Fig. 9 displays the comparison between the measured and simulated magnetic field projected for the most compatible magnetization

configuration displayed in Fig. 4i. Other simulated magnetic configurations were found to radiate a magnetic field in qualitative agreement with the measured one (Supplementary Fig. 10 and Supplementary Fig. 11). Fig. 4g-i sum up the multiferroic topological states deduced from simulations for both the as-grown ferroelectric stripes as well as the written divergent and convergent center states.

Repeating the writing process identically on multiple disk-shaped devices did not necessarily yield identical net magnetization configurations. The magnetoelectric coupling then appears less deterministic for the G-type antiferromagnetic ordering than for the bulk-like cycloidal one. However, evidence suggests that the net magnetization direction lies along either $\pm[-211]$ or $\pm[1-21]$ (for a ferroelectric polarization oriented along $[111]$), and actually never occurs along the $\pm[11-2]$ variant. In terms of their respective associated antiferromagnetic vectors, it means that only the out-of-plane $[0-11]$ or $[10-1]$ are favored, and the $[-110]$ one lying strictly in the thin film plane is discarded (Supplementary Fig. 4). This is in line with Landau-Ginzburg theory predicting that compressive epitaxial strain should favor spins in the (001) film plane while tensile strain leads to out-of-plane spins²⁶.

We now focus on the nature of the antiferromagnetic domain boundaries embedded in these different polar textures. The identification of the M domains in each polar configuration allows us to determine the direction of the Néel vectors. As we cannot distinguish antiphase boundaries, we define L_i as green double arrows in Fig. 4g-i. In the as-grown striped domain structure, the ferroelectric domain walls always coincide with antiferromagnetic domain walls, defining them as multiferroic domain walls³⁰. In addition, pure antiferromagnetic domain walls can be identified within the ferroelectric stripes (Supplementary Fig. 12a). In the electric-field induced center polar states, these multiferroic domain walls are accompanied by pure

ferroelectric domain walls through which the antiferromagnetic Néel vector is preserved (Supplementary Fig. 12b-c). These observations of purely ferroelectric, purely antiferromagnetic, or multiferroic domain walls are reminiscent of the seminal papers from M. Fiebig et al. on other multiferroic compounds^{30–32}. Thus, although tensile strain promoting pseudo collinear antiferromagnetism prevents a fully deterministic control of the canted antiferromagnetic state via the magnetoelectric coupling, it still allows for the discrimination of several net magnetization configurations, with a rich zoology of embedded antiferromagnetic domains and domain walls, paving the path for further study of this magnetoelectric coupling in such exotic and largely unexplored G-type antiferromagnetic thin films with different crystalline orientations.

Discussion

In this work, we reported the successful design and writing of two different families of multiferroic topological entities. The first set was obtained on BiFeO₃ epitaxial thin films subjected to compressive strain, and consist in antiferromagnetic vortices induced by spin cycloids coupled to ferroelectric center domains. The second was achieved on similar films subjected to tensile strain, and amount to four-quadrant canted G-type antiferromagnetic domains imprinted from ferroelectric center domains.

In the first case, epitaxial strain discriminates the spin cycloids propagation directions permitted by magnetoelectric coupling, and yields only the direction lying strictly in the sample plane. In the second case, it also discriminates the allowed antiferromagnetic vectors, resulting in the prohibition of the one lying strictly in the sample plane.

All multiferroic textures discussed in this work were written by simple electric pulses from their as-grown state, and can be switched from the center-convergent to the center-divergent

ferroelectric states by reversing the voltage sign. Doing so reverses the spin cycloid vortex rotation in the case of compressive strain, or changes the net four-quadrant magnetization configuration in the case of tensile strain. Such a switchable behavior may lay the foundations for topological multiferroic memories.

Acknowledgements

We are grateful to Nicolas Reyren for fruitful discussions. We are thankful for support from the French Agence Nationale de la Recherche (ANR) through the project TATOO (ANR-21-CE09-0033) and ESR/EquipEx+ program e-DIAMANT (Grant No. ANR-21-ESRE-0031), the European Union's Horizon 2020 research and innovation programme under the Grant Agreements No. 964931 (TSAR) and No. 866267 (EXAFONIS). This work is supported by a public grant overseen by the ANR as part of the "Investissements d'Avenir" program (Labex NanoSaclay, reference: ANR-10-LABX-0035). The Sesame Ile de France IMAGESPIN project (No. EX039175) is also acknowledged.

Authors contributions

V.G. and S.F. designed the experiments. V.G. coordinated the work. P.D., A.A. and J.F. synthesized the thin films by pulsed laser deposition. S.F. and S.C. fabricated the devices using e-beam lithography and sputtering deposition. A.C. switched and examined the polar textures using piezoresponse force microscopy. A.C. investigated the coupled spin textures using scanning NV magnetometry with the help of K.B. Z.L., J.-Y.C., and M.V. performed the atomic spin simulations. A.F. and V.J. performed the micromagnetic simulations. A.C., S.F. and V.G. wrote the core of the manuscript. All the authors discussed the results and contributed to the manuscript preparation.

Competing interests

The authors declare no competing interests

Figure captions

Fig. 1. Concept of multiferroic topological states. **a** and **c**, Sketches illustrating the convergent (**a**) and divergent (**c**) center polar (white arrows) states. **b**, Atomic force microscopy topography of the device geometry with lateral PFM phase signal overlaid. The bright (dark) color corresponds polarization pointing to frontside (back side) as sketched in the inset. Two holes (1 μm diameter in a 30 nm thick Pt line) on the left (right) of the AFM tip were poled with negative (positive) bias, the other holes correspond to pristine domains. **d** and **g**, Sketches illustrating a four-quadrant center polar texture with associated antiferromagnetic clockwise (**d**) and counter-clockwise (**g**) spin rotations (blue and red arrows stand for the antiferromagnetic spins), given the single magnetic polarity of the spin cycloid. **e** and **f**, Zoomed-in computed spin textures at the core of the ‘geometrically perfect’ center domains showing antiferromagnetic hedgehog antivortices (**e**) and vortices (**f**) for the convergent and divergent cases, respectively. The color scale displays the z-component of the Néel vectors.

Fig. 2. Polar maps extracted from piezoresponse force microscopy. PFM characterization of an upwards center-convergent ferroelectric texture written by a +60 V pulse. **a**, Topography (color bar in nm). **b**, Vertical piezoresponse extracted from the cantilever deflection. **c-d**, Lateral piezoresponse extracted from the cantilever torsion, for different angles of the sample with respect to the cantilever direction. Color bars in **b-d** in arbitrary units. The insets on the bottom left of **a-c** show the cantilever orientation during measurement. **e**, 3D sketch of the resulting polar configuration, considering a single polarization in each quadrant. **f**, 2D in-plane piezoresponse vector map of the area indicated by a circle, extracted pixelwise by trigonometric regression on all lateral piezoresponse images measured for different cantilever orientations. Vector lengths and directions show the local magnitude and direction of the surface in-plane deformation. The overlapped color map provides the projection of this direction

on the closest crystallographic axes permitted for the ferroelectric polarization. The color bar displays the corresponding angle θ , as defined from the sketch. Scale bars are 200 nm.

Fig. 3. Magnetoelectric coupling in ferroelectric center states written on a (001)-oriented 33-nm-thick BiFeO₃ thin film under -0.35% compressive strain. Scale bars are 100 nm. **a-c**, Piezoresponse vector maps and underlying ferroelectric textures for the as-grown (a), downwards center-divergent (b) and upwards center-convergent (c) states. The insets display a 3D sketch of the polar configuration. **d-f**, Schematics of the associated multiferroic topological states. The cycloid propagation vectors are depicted as green double arrows. Considering a single magnetic polarity in each domain results in opposite spin cycloid vortex helicities around the core of center-divergent and center-convergent polar states, as depicted by the center-convergent and center-divergent magnetic polarities λ . **g-i**, Out-of-plane magnetic field radiated by the antiferromagnetic textures from NV magnetometry (dark lines highlight the ferroelectric domain walls). **j-k**, Spin-level simulations of the antiferromagnetic textures, initialized with the ferroelectric domains extracted from experimental measurements. The computed out-of-plane magnetic field is displayed, as well as a zoom in the core configuration of the antiferromagnetic spins.

Fig. 4. Magnetoelectric coupling in ferroelectric center states written on a (001)-oriented 32-nm-thick BiFeO₃ thin film grown under +0.50% tensile strain. Scale bars are 100 nm. **a-c**, Piezoresponse vector maps and underlying ferroelectric textures for the as-grown (a), downwards center-divergent (b) and center-convergent (c) states. The insets display a 3D sketch of the polar configuration. **d-f**, Associated magnetic field radiated by the antiferromagnetic textures from NV magnetometry (dark lines highlight the ferroelectric domain walls). **g-i**, Schematics of the resulting multiferroic states: red and purple vectors show the in-plane projections of polarization and the weak moment stemming from the canting of the G-type antiferromagnetic spins. The green double arrows indicate the corresponding

Néel vectors. All magnetization configurations allowed by magnetoelectric coupling were simulated and compared, with the ones selected here yielding the best fit to experimental data.

References

1. Junquera, J. *et al.* Topological phases in polar oxide nanostructures. *Rev Mod Phys* **95**, 025001 (2023).
2. Yadav, A. K. *et al.* Observation of polar vortices in oxide superlattices. *Nature* **530**, 198–201 (2016).
3. Das, S. *et al.* Observation of room-temperature polar skyrmions. *Nature* **568**, 368–372 (2019).
4. Zhang, Q. *et al.* Nanoscale Bubble Domains and Topological Transitions in Ultrathin Ferroelectric Films. *Adv. Mater.* **29**, 1702375 (2017).
5. Han, L. High-density switchable skyrmion-like polar nanodomains integrated on silicon. **603**, 63–67 (2022).
6. Kim, K.-E. *et al.* Configurable topological textures in strain graded ferroelectric nanoplates. *Nat. Commun.* **9**, 403 (2018).
7. Ma, J. *et al.* Controllable conductive readout in self-assembled, topologically confined ferroelectric domain walls. *Nat. Nanotechnol.* **13**, 947–952 (2018).
8. Yang, W. *et al.* Quasi-one-dimensional metallic conduction channels in exotic ferroelectric topological defects. *Nat. Commun.* **12**, 1306 (2021).
9. Li, Z. *et al.* High-density array of ferroelectric nanodots with robust and reversibly switchable topological domain states. *Sci. Adv.* **3**, e1700919 (2017).
10. Han, M.-J. *et al.* Shape and Surface Charge Modulation of Topological Domains in Oxide Multiferroics. *J. Phys. Chem. C* **123**, 2557–2564 (2019).
11. Yang, W. *et al.* Nonvolatile Ferroelectric-Domain-Wall Memory Embedded in a Complex Topological Domain Structure. *Adv. Mater.* **34**, 2107711 (2022).
12. Mermin, N. D. The topological theory of defects in ordered media. *Rev. Mod. Phys.* **51**, 591–648 (1979).
13. Gross, I. *et al.* Real-space imaging of non-collinear antiferromagnetic order with a single-spin magnetometer. *Nature* **549**, 252–256 (2017).
14. Sosnowska, I., Neumaier, T. P. & Steichele, E. Spiral magnetic ordering in bismuth ferrite. *J. Phys. C Solid State Phys.* **15**, 4835–4846 (1982).
15. Lebeugle, D. *et al.* Electric-Field-Induced Spin Flop in BiFeO₃ Single Crystals at Room Temperature. *Phys. Rev. Lett.* **100**, 227602 (2008).
16. Burns, S. R., Paull, O., Juraszek, J., Nagarajan, V. & Sando, D. The Experimentalist's Guide to the Cycloid, or Noncollinear Antiferromagnetism in Epitaxial BiFeO₃. *Adv. Mater.* **32**, 2003711 (2020).
17. Haykal, A. *et al.* Antiferromagnetic textures in BiFeO₃ controlled by strain and electric field. *Nat. Commun.* **11**, 1704 (2020).
18. Zhong, H. *et al.* Quantitative Imaging of Exotic Antiferromagnetic Spin Cycloids in BiFeO₃ Thin Films. *Phys. Rev. Appl.* **17**, 044051 (2022).
19. Finco, A. *et al.* Imaging Topological Defects in a Noncollinear Antiferromagnet. *Phys. Rev. Lett.* **128**, 187201 (2022).
20. Waterfield Price, N. *et al.* Electrical Switching of Magnetic Polarity in a Multiferroic BiFeO₃ Device at Room Temperature. *Phys. Rev. Appl.* **8**, 014033 (2017).
21. Johnson, R. D. *et al.* X-Ray Imaging and Multiferroic Coupling of Cycloidal Magnetic Domains in Ferroelectric Monodomain BiFeO₃. *Phys. Rev. Lett.* **110**, 217206 (2013).
22. Waterfield Price, N. *et al.* Strain Engineering a Multiferroic Monodomain in Thin-Film BiFeO₃. *Phys. Rev. Appl.* **11**, 024035 (2019).
23. Thiaville, A., Miltat, J. & Rohart, S. 1 - Magnetism and topology. in *Magnetic Skyrmions and*

- Their Applications* (eds. Finocchio, G. & Panagopoulos, C.) 1–30 (Woodhead Publishing, 2021).
doi:10.1016/B978-0-12-820815-1.00012-2.
24. Park, M. *et al.* Three-dimensional ferroelectric domain imaging of epitaxial BiFeO₃ thin films using angle-resolved piezoresponse force microscopy. *Appl. Phys. Lett.* **97**, 112907 (2010).
 25. Chen, Z. H., Damodaran, A. R., Xu, R., Lee, S. & Martin, L. W. Effect of “symmetry mismatch” on the domain structure of rhombohedral BiFeO₃ thin films. *Appl. Phys. Lett.* **104**, 182908 (2014).
 26. Sando, D. *et al.* Crafting the magnonic and spintronic response of BiFeO₃ films by epitaxial strain. *Nat. Mater.* **12**, 641–646 (2013).
 27. Agbelele, A. *et al.* Strain and Magnetic Field Induced Spin-Structure Transitions in Multiferroic BiFeO₃. *Adv. Mater.* **29**, 1602327 (2017).
 28. Chauleau, J.-Y., Haltz, E., Carrétéro, C., Fusil, S. & Viret, M. Multi-stimuli manipulation of antiferromagnetic domains assessed by second-harmonic imaging. *Nat. Mater.* **16**, 803–807 (2017).
 29. Ederer, C. & Spaldin, N. A. Weak ferromagnetism and magnetoelectric coupling in bismuth ferrite. *Phys. Rev. B* **71**, 060401 (2005).
 30. Fiebig, M., Lottermoser, Th., Fröhlich, D., Goltsev, A. V. & Pisarev, R. V. Observation of coupled magnetic and electric domains. *Nature* **419**, 818–820 (2002).
 31. Meier, D. *et al.* Topology and manipulation of multiferroic hybrid domains in MnWO₄. *Phys. Rev. B* **80**, 224420 (2009).
 32. Fiebig, M., Lottermoser, T., Meier, D. & Trassin, M. The evolution of multiferroics. *Nat. Rev. Mater.* **1**, 16046 (2016).

426 **Methods**

427

428 **Sample fabrication**

429 BiFeO₃ thin films were grown by pulsed laser deposition on DyScO₃(110) and SmScO₃(110)
430 orthorhombic substrates using a KrF excimer laser (248 nm), as detailed in Ref. 17.

431

432 **Top electrode patterning**

433 The 15-nm-thick Pt electrode was deposited by sputtering after performing an electronic
434 beam lithography to induce nanostructures of various geometries and sizes where BiFeO₃ is
435 left bare. Disk shaped devices were found to host the most accurate and reproducible
436 ferroelectric center domains after electric pulse writing, exhibiting clear monodomains in each
437 of the quadrants, as well as low roughness and straight domain walls. Diameters of around
438 800 nm were used to keep the devices as small as possible while allowing the 200-nm-wide
439 NV-center diamond tip to come in contact with the BiFeO₃ surface over an area large enough
440 for proper imaging.

441

442 **Writing of center domains**

443 Ferroelectric center states were induced through electrical interaction between a conductive
444 tip and the patterned top electrode. While the tip was grounded and stationed in direct
445 contact with BiFeO₃ at the center of an 800 nm disk pattern, a DC pulse of around +50 V or -
446 50 V was applied on the surrounding electrode to write a head-to-head or tail-to-tail center
447 domain respectively. Pulse duration was not found to have any significant impact beyond a
448 few milliseconds, and was therefore set around 100 ms.

449

Piezoresponse force microscopy

The experiments were conducted with an atomic force microscope (Nanoscope V multimode, Bruker) and two external lock-in amplifier detectors (SR830, Stanford Research) for the simultaneous acquisition of lateral and vertical piezoresponses. An external ac source (DS360, Stanford Research) was used to excite the Pt patterned top electrode at a frequency of 35 kHz while the conducting Pt-coated tip was grounded. We used stiff cantilevers (40 N m^{-1}) for accurate vertical detection and softer ones (7 N m^{-1}) for the lateral detection. Regarding the as-grown state, BiFeO_3 on SmScO_3 exhibits a homogeneous vertical signal, corresponding to a polarization pointing upwards, i.e. away from the substrate, while BiFeO_3 on DyScO_3 exhibits a quasi-homogeneous vertical signal, corresponding to a polarization pointing downwards, i.e. towards the substrate. All images were obtained with phase shifts close to 180 degrees between in-plane domains, as well as between out-of-plane domains.

Scanning NV magnetometry

Experiments were performed using a commercial scanning N-V magnetometer (Qnami, ProteusQ) operated under ambient conditions, with commercial all-diamond scanning-probe tips containing single NV defects (Qnami, Quantilever MX). The tip was integrated into a tuning-fork based atomic force microscope combined with a confocal microscope optimized for single NV defect spectroscopy. Magnetic fields radiated by the sample are detected by recording the Zeeman shift of the NV defect's electronic spin sublevels through optical detection of the electron spin resonance.

The scanning NV magnetometer was operated in the full-B imaging mode by continuously monitoring the photoluminescence (PL) intensity and sweeping the applied microwave frequency (ν) at each point of the scan. A Lorentzian fit on $\text{PL}(\nu)$ then provides the

aforementioned local resonance frequency. Experiments were performed with a NV-to-sample distance of approximately 50 nm and a bias magnetic field of 1 mT applied along the NV quantization axis. Thermal drift was a significant source of error in our slow full-B quantitative measurements, therefore all textures were also imaged in the faster dual-iso-B mode to confirm the overall patterns with limited drift.

Extraction of 3D magnetic field

Full-B NV-center magnetometry provides a quantitative measure of the magnetic field radiated at the defect's height and along the defect's symmetry axis. Making use of Maxwell's equations in air in the absence of currents and time-dependent electric fields, $\nabla \cdot \mathbf{B} = 0$ and $\nabla \times \mathbf{B} = \mathbf{0}$, one can compute the two remaining components of \mathbf{B} perpendicular to the symmetry axis. This computation was simplified by assuming a uniform absolute height of the NV-center over the whole measured area. The resulting 3D magnetic field was then projected along all three sample axes, and either all projections or the most relevant one are displayed here, although it should be noted that a single projection already holds the full information.

Data noise filtering

Most piezoresponse and magnetometry images were filtered by Gaussian kernels whose standard deviations were kept lower than the about 10 nm lateral resolution of the scanning probe microscopes. Such filters were applied on the X-Y coordinates of the piezoresponse before converting them into R- θ .

Four-quadrant spin cycloid simulations

497 Simulating antiferromagnetic textures on a large scale remains a challenging task because of
498 the large number of involved magnetic moments. Indeed, they have to be performed on the
499 atomic level in order to grasp a realistic picture of their magnetic properties. For this work,
500 atomic spin simulations have been performed using a GPU based home-made code. This code
501 is based on solving the Landau-Lifschitz-Gilbert equation for every atomic magnetic moment.
502 In order to reproduce the BiFeO₃ spin textures, the effective Hamiltonian includes all relevant
503 energy terms as described in Ref. 33. The main ones are: the direct antiferromagnetic
504 exchange which favors the antiparallel alignment of spins, the magneto-electric coupling
505 which promotes the stabilization of the antiferromagnetic cycloid, the “alternating” second
506 DMI term which is responsible for the emergence of the spin density wave. Besides, two
507 anisotropy terms are also needed namely a uniaxial easy-axis anisotropy long direction of the
508 electric polarization, i.e. one of the [111] directions, and a weaker 6-fold anisotropy in the
509 perpendicular plane. All parameters have been taken from Ref. 34. However, for the sake of
510 computing time, the magnetoelectric amplitude has been increased by a factor 10 which leads
511 to a shortening of the period of antiferromagnetic cycloid. It therefore allowed to simulate
512 smaller volumes, yet keeping a qualitative agreement.

513 In the present work, the simulations have been performed for a 120 nm × 120 nm square (in
514 the [100] and [010] directions respectively) and for a thickness of 0.78 nm (in the [001]
515 direction) which corresponds to 303 × 303 × 2 atomic magnetic moments. Noteworthy, while
516 boundary conditions are periodic in the [001] direction, they are let free in the in-plane
517 directions. Indeed, in the presence of the spin cycloid, periodic boundary conditions in these
518 directions could be more detrimental than free boundary condition and non-negligibly affect
519 the cycloid properties. In our case, the borders are far enough so that the region of interest is
520 unaffected. The 4-quadrant electrical landscape is reproduced by defining four regions with

corresponding orientations of the magneto-electric term and the DMI term. The initialization conditions are the expected antiferromagnetic cycloid properties far from the ferroelectric domain walls which are subsequently relaxed to obtained

In order to compare the atomic simulations to the scanning NV magnetometry images, the magnetic fringing field has been computed in a standard way. However, the period of the antiferromagnetic spin cycloid being 10 times shorter, the magnetic field has been mapped at a 5 nm height from the sample surface, i.e. typically 10 times closer than in the NV-center measurements.

Four-quadrant net magnetization simulations

The simulations of the magnetic stray field resulting from the G-type antiferromagnetic quadrants were done assuming that only the canted moments are contributing (more information in Supplementary Note 1). These moments can have 3 possible directions with respect to P, as shown in Supplementary Fig. 4, and considering that their sign is unknown, we end up to 6 possible directions of M in each quadrant. Finally, the whole number of possible configurations is thus 6^4 .

The magnetic state used for each simulation corresponds to 4 domains with boundaries extracted from the PFM data, and in each domain one of the 6 possible orientations of M for the associated direction of P.

The stray field maps are then obtained by separating the magnetic sample in 5 nm x 5 nm cells and summing up the contribution of each cells at every position of the map, using the method described in Ref. 35.

Sample and device statistics

545 Piezoresponse force microscopy data displayed in Fig. 3a-c for the as-grown, center-divergent,
546 center-convergent polar states, respectively, were collected on three different devices of the
547 same $5 \times 5 \text{ mm}^2$ Pt/BiFeO₃/DyScO₃ sample. The very same devices were imaged by scanning
548 NV magnetometry in Fig. 3g-i. Piezoresponse force microscopy data displayed in Fig. 4a-c for
549 the as-grown, center-divergent, center-convergent polar states, respectively, were collected
550 on three different devices of the same $5 \times 5 \text{ mm}^2$ Pt/BiFeO₃/SmScO₃ sample. The very same
551 devices were imaged by scanning NV magnetometry in Fig. 4d-f. The polar configurations
552 displayed in Fig. 1, 2, 3, 4 were reproduced on at least 20 devices for the two different samples.
553
554

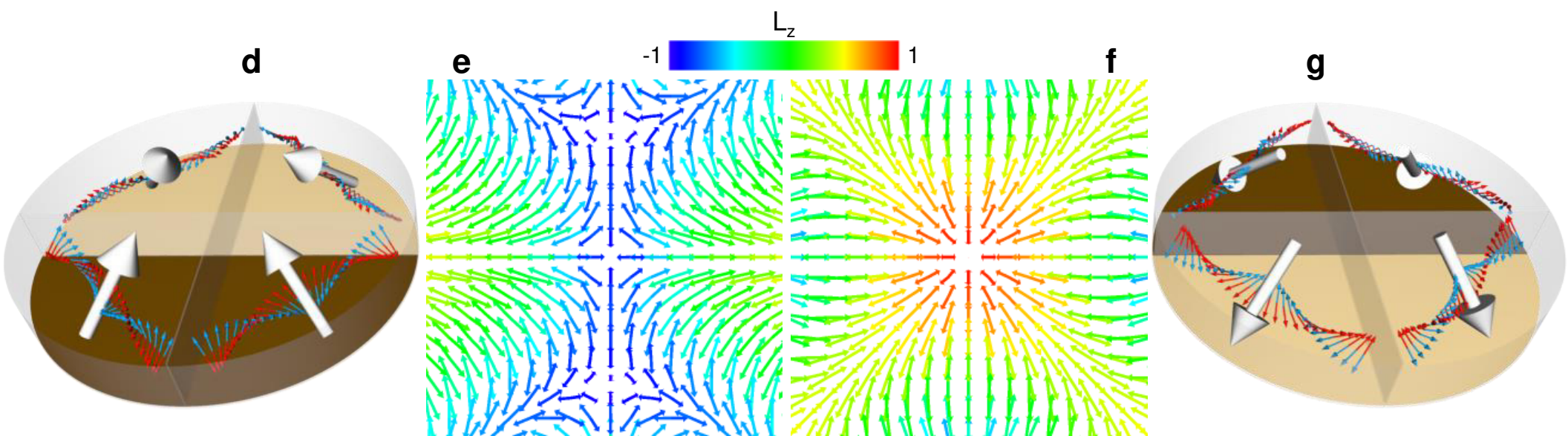
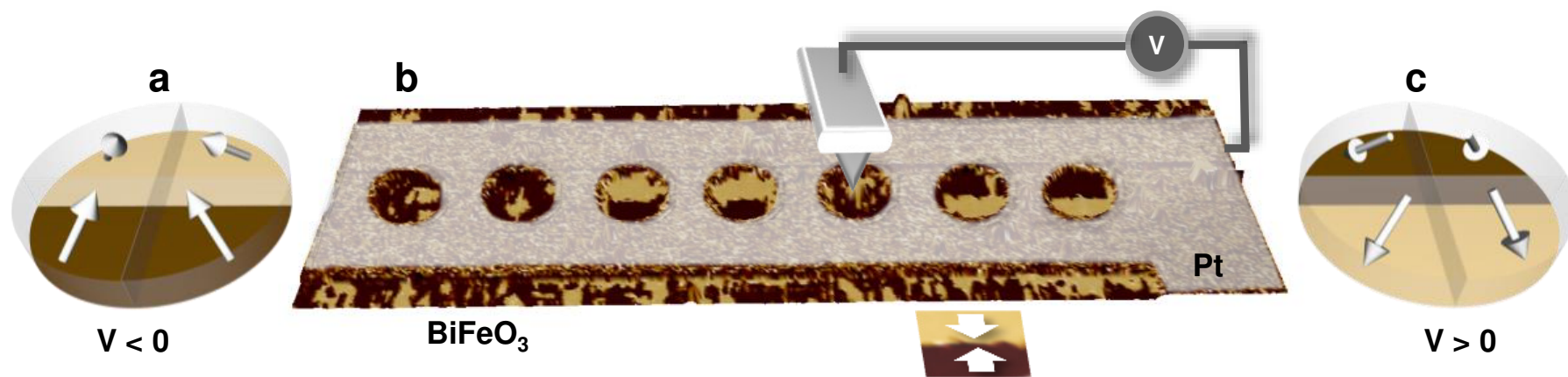
555 **Data availability**

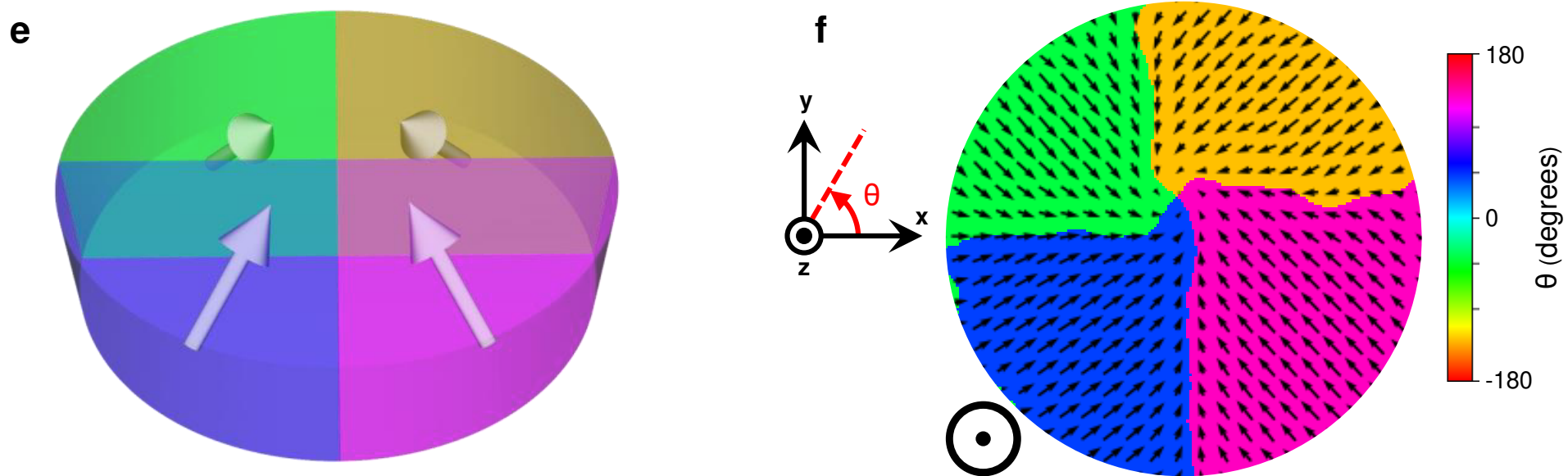
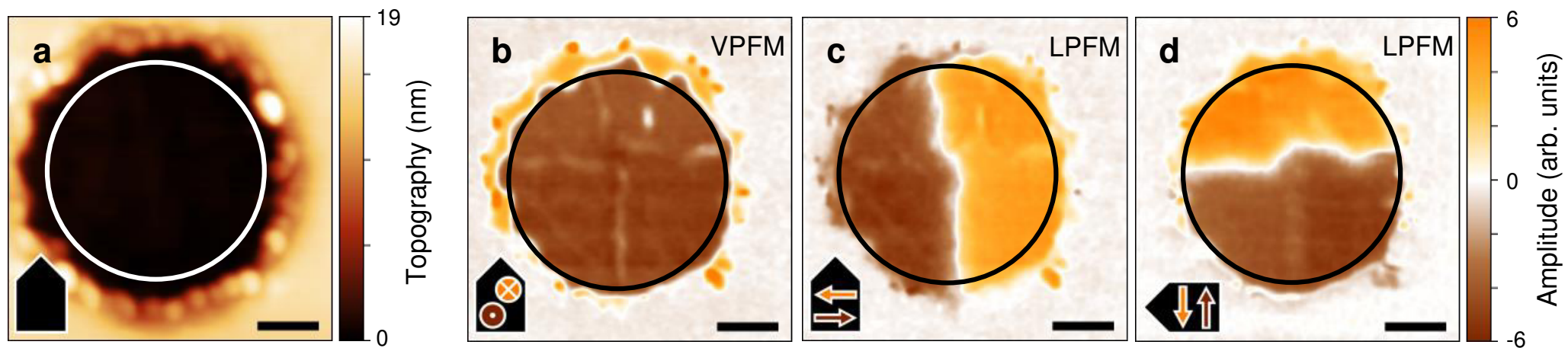
556 The data that support this work are available in <https://zenodo.org/records/10875992>.

557

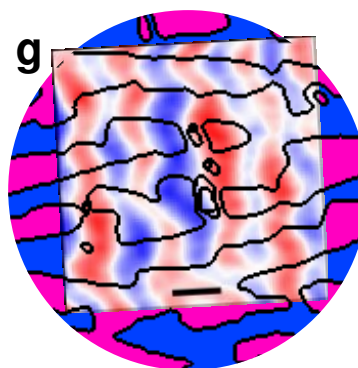
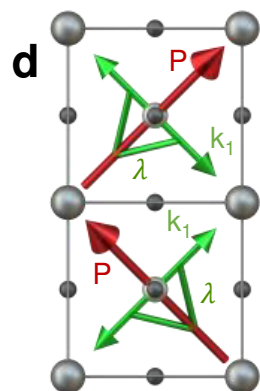
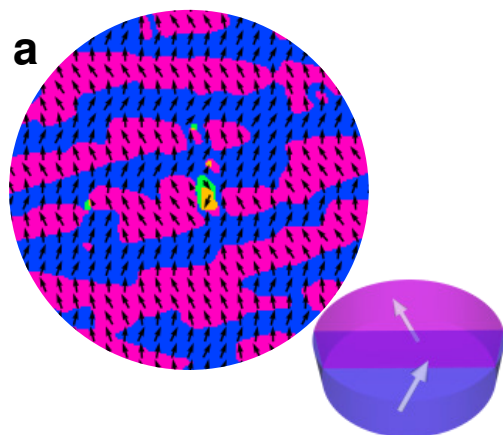
558 **Methods-only references**

- 559 33. Li, Z. *et al.* Multiferroic skyrmions in BiFeO₃. *Phys. Rev. Res.* **5**, 043109 (2023).
560 34. Fishman, R. S. The microscopic model of BiFeO₃. *Phys. B* **536**, 115–117 (2018).
561 35. Abert, C., Selke, G., Kruger, B., & Drews, A. A Fast Finite-Difference Method for
562 Micromagnetics Using the Magnetic Scalar Potential. *IEEE Trans. Magn.* **48**, 1105–1109 (2012).
563

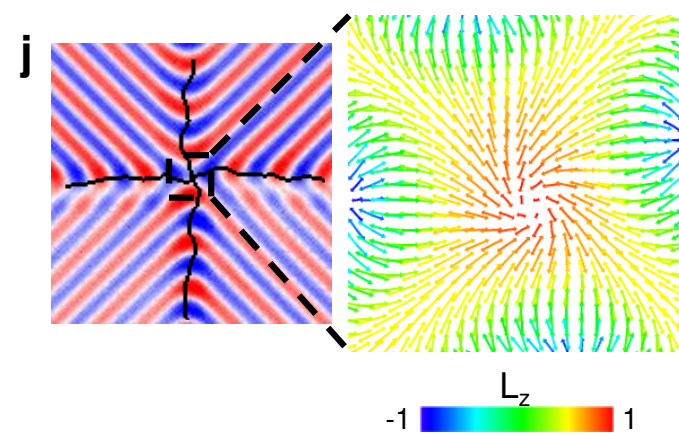
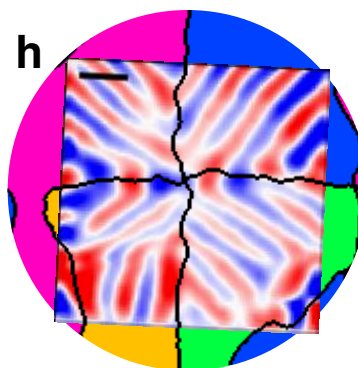
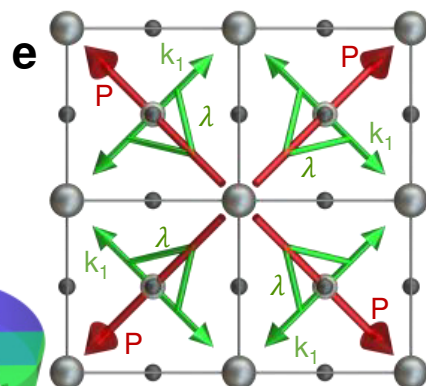
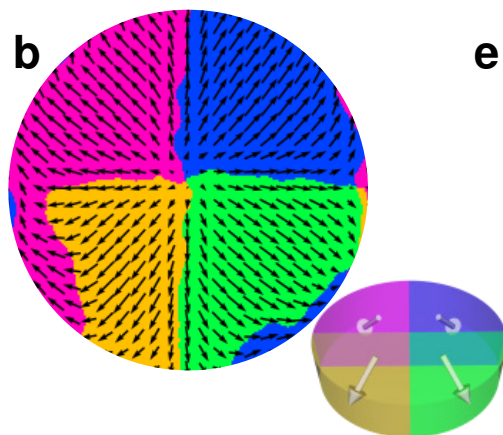




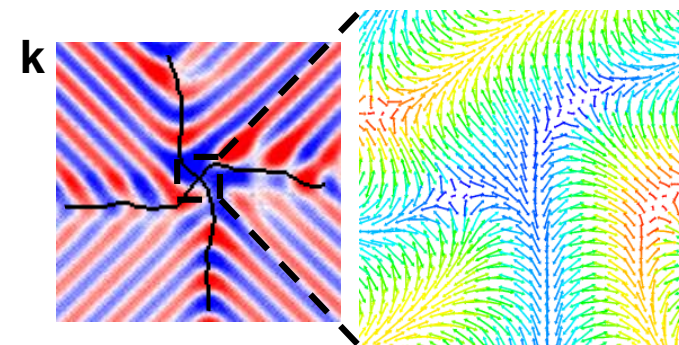
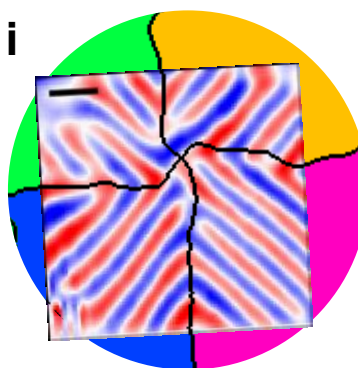
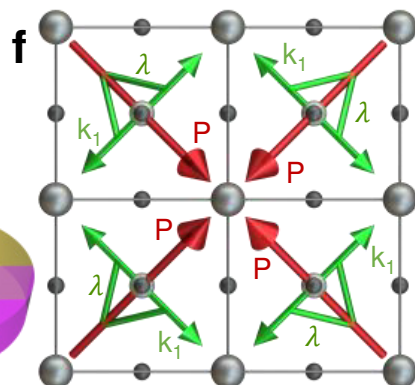
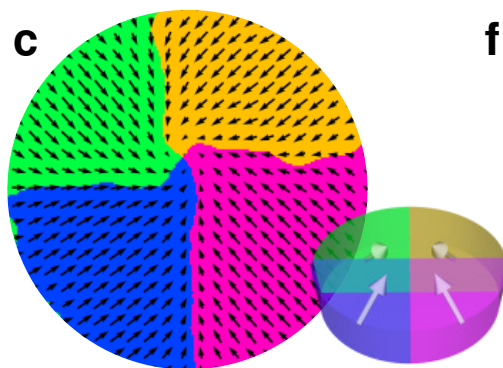
As-grown



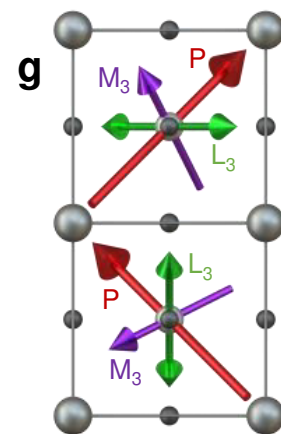
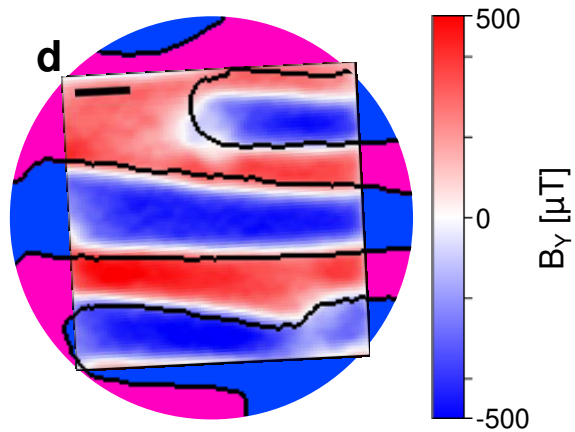
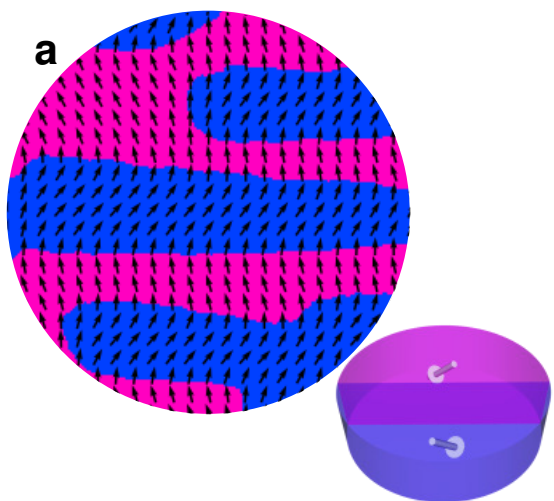
Center-divergent



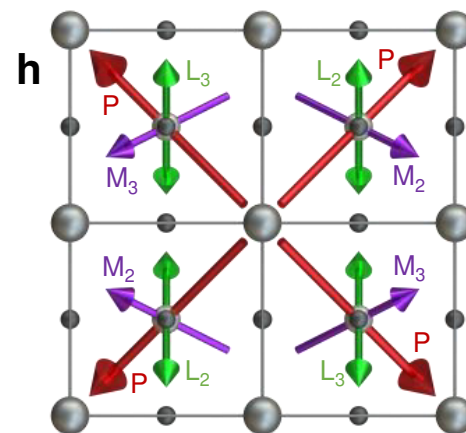
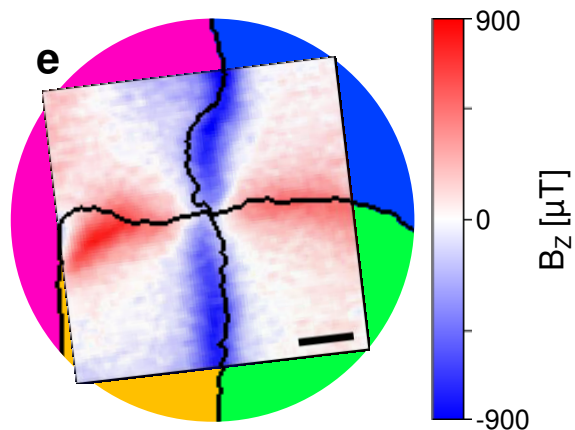
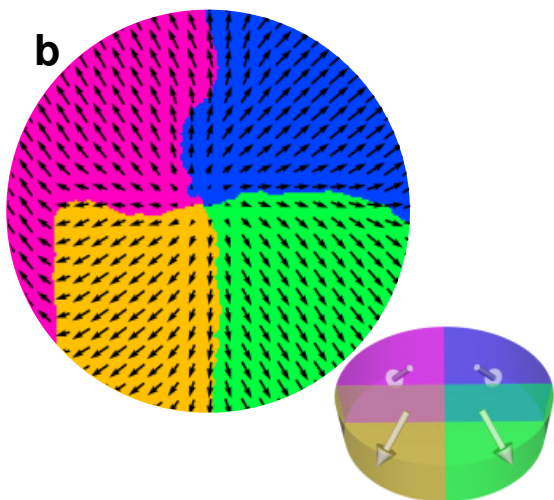
Center-convergent



As-grown



Center-divergent



Center-convergent

